Fuel 345 (2023) 128064

Contents lists available at ScienceDirect

Fuel

journal homepage: www.elsevier.com/locate/fuel

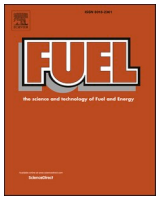

Full Length Article

Computational study of the multidimensional spread of smouldering combustion at different peat conditions

Han Yuan [a,c], Dwi M.J. Purnomo [a,b], Peiyi Sun [c], Xinyan Huang [c], Guillermo Rein [a,*]

[a] Department of Mechanical Engineering, Imperial College London, Exhibition Road, London SW7 2AZ, UK
[b] Department of Mechanical Engineering, University of California Berkeley, Berkeley, CA 94720, USA
[c] Research Centre for Fire Safety Engineering, The Hong Kong Polytechnic University, Kowloon, Hong Kong Special Administrative Region

ARTICLE INFO

Keywords:
Smouldering combustion
Biomass
Multi-dimensional
Numerical simulation
Fire spread rate

ABSTRACT

Smouldering combustion is the slow, low-temperature, flameless burning of porous fuels, which propagate both laterally and in-depth. In this study, we build a physics-based two-dimensional model to simulate lateral and in-depth smouldering spread simultaneously based on open-source code Gpyro. We first validate the model against a shallow-reactor experiment (of 1.6 cm thickness) in the literature. Based on the validated model, we then investigate 2D smouldering in a 3 times deeper peat layer at different soil conditions. We found that lateral and in-depth spread rates depend on the organic density and the Oxygen supply. Because of the larger Oxygen supply close to the free surface, the lateral spread is 10 times faster than in-depth spread. In addition, for lateral spread the influence of inorganic density and moisture can be explained by a unified parameter, heat sink density, agreeing with previous experimental results. The model predicts the effects of peat conditions on multidimensional smouldering spread and reveals the controlling mechanisms both lateral and in-depth spread, providing a better understanding of this complex phenomenon.

1. Introduction

Smouldering peat wildfires release carbon stored in peat, thus resulting in a positive feedback that serves to advance climate change [1]. Smouldering is the slow, low-temperature, flameless burning of porous fuels [2]. It is sustained by the heat produced when oxygen directly attacks the surface of the solid fuel [1]. Thus, smouldering is a complex heterogeneous process, where chemistry, heat transfer and mass transfer occur simultaneously [3]. Peat, as typical organic soil, is a porous and charring natural fuel, thus prone to smouldering. Once ignited, smouldering peat wildfires can persist for days to months, despite rainfall and firefighting attempts. These wildfires can release huge amounts of carbon; in 1997, peat wildfires in Southeast Asia emitted 0.8–2.56 Gt-C to the atmosphere, equivalent to 13–40% of the global anthropogenic carbon emissions in that year [4–6].

Moisture content (MC, the amount of water in the soil), inorganic content (IC, the quantity of non-combustible material), and organic density are the three most influential factors (in that order) on ignition, propagation, and extinction behaviour of smouldering peat wildfires [7–12]. The propagation of smouldering is a multi-dimension process, where the lateral spread is along the peat layer, and in-depth spread is into the bulk of the peat [2]. Previous studies have been conducted to study the influence of peat conditions on either lateral spread or in-depth spread. Laboratory experiments [10,13] have found that the lateral spread rate decrease with moisture, because more energy and time are required to dry the peat. Peat with a relatively high MC (but still below critical MC) can smoulder[14,15], and lateral spread rates are faster a few centimetres below the surface, forming an overhang [13]. Huang and Rein [16] found that in-depth spread rate increases with MC because of the smaller organic density. On the other hand, IC slightly decreases in-depth spread, according to both experiments and modelling [9,17]. Most previous studies are experimental. Computational studies are limited and focused on either lateral spread only [18] or in-depth spread only [8,9,16,19]. The literature lacks a computational study to investigate the multi-dimensional smouldering dynamics that combines both lateral spread and in-depth spread simultaneously, which is the phenomenon that actually happens.

To fill this knowledge gap, this paper builds a two-dimensional physics-based model to simulate smouldering combustion in peat. The model is first validated against shallow-reactor experiments in the literature. Based on the validated model, we further simulate the two-dimensional smouldering combustion of a thicker peat layer, reveal the controlling mechanisms for two types of spreads, and investigate the

* Corresponding author.
E-mail address: g.rein@imperial.ac.uk (G. Rein).

https://doi.org/10.1016/j.fuel.2023.128064
Received 10 June 2022; Received in revised form 21 February 2023; Accepted 3 March 2023
Available online 23 March 2023

Nomenclature

Symbols

A	pre-exponential factor,1/s
c	specific heat capacity, J/kg-K
D	mass diffusivity, m^2/s
E	activation energy, kJ/mol
$\bar{h}$	specific enthalpy, J/kg
h_c	convective heat transfer coefficient, W/m^2-k
h_m	diffusive mass-transfer coefficient, kg/m^2-s
ΔH	change in enthalpy, MJ/kg
k	thermal conductivity, W/m-k
L	the depth of sample, mm
$\dot{m}''$	mass flux, kg/m^2-s
M	molecular mass, g/mol
n	heterogeneous reaction order
P	pressure, Pa
t	time, s
T	temperature, ℃
x	horizontal distance, mm
Y	mass fraction
z	vertical distance, mm

Greeks

ε	emissivity
κ	permeability, m^2
$\bar{\rho}$	bulk density, kg/m^3
ν	viscosity/stoichiometry
ϕ	porosity
$\dot{\omega}$	reaction rate, 1/s
$\dot{\omega}''$	volumetric reaction rate, kg/m^3-s
σ	weighted collision diameter, Å

Subscripttts

0	initial
a	ash
f	formation
d	destruction
g	gas
i	inorganic matters/solid species index
j	gaseous species index
k	reaction index
N	nitrogen
O	oxygen
p	peat
w	water
∞	free surface

influence of peat conditions.

2. Computational model

We used the experiments of Christensen et al. [10] to validate our model, which the best experiments in the literature for lateral spread; thus, a brief introduction of the experimental study of Christensen et al. [10] is given here. The dimensions of this shallow reactor are 40 × 40 × 1.6 [cm] (Fig. 1). The reactor was built using insulating ceramic boards (k = 0.7 $W.m^{-1}K^{-1}$, ρ = 310 $kg.m^{-3}$, c = 1090 $J.kg^{-1}K^{-1}$). Commercial milled Irish Sphagnum peat of dry density 158 ± 15 kg/m^3 and inherent inorganic content (IC) of 2.5 ± 0.6% was used [10].

Both IC and MC were calculated on a dry basis (Eqs. (1) and (2)), where m_w is the mass of the water, m_s is the mass of the added sand, IC_0 is the inherent inorganic content of the unconditioned peat (~2.5%), and m_p is the mass of the unconditioned peat. Samples with different ICs and MCs were ignited at the centre with 20 W for 30 min as the ignition protocol. Christensen et al. [10] studied in-depth and lateral spread rates as well as smouldering width. The experiment under each IC and MC combination in Christensen et al. [10] was repeated three times to obtain the experimental uncertainty.

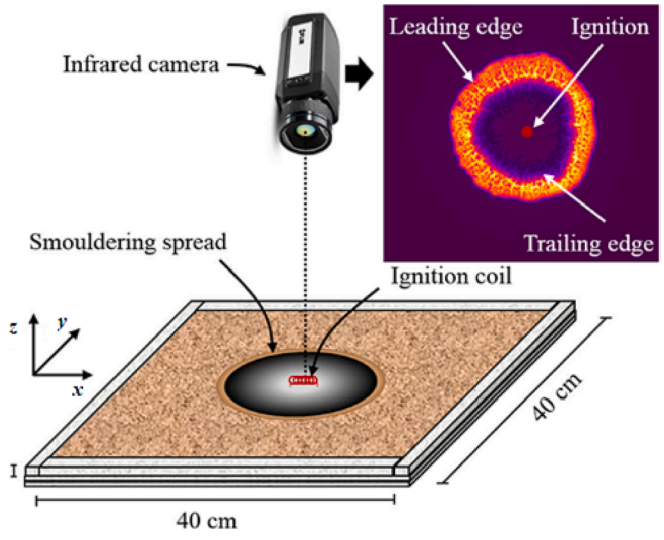

Fig. 1. Illustration of the experimental setup in Christensen et al. [10], displaying a central ignition using a wound coil and key features observable in IR imaging.

$$MC = \frac{m_w}{m_p + m_s}\% \tag{1}$$

$$IC = \frac{m_s + IC_0 m_p}{m_s + m_p} \tag{2}$$

2.1. Governing equations and chemical kinetics

Our computational model was sbuilt on Gpyro [20]. Gpyro is an open-source code that integrates mechanisms of mass transfer, heat transfer, and chemistry for reactive porous media and has a robust inbuilt stiff solver capable of solving complex smouldering problems [20,21]. The governing equations used in this study impose conservations of Eqs. (3) mass, (4) species and (5) energy in the solid phase, as well as (6) mass, (7) species, and (8) momentum (Darcy's law) in the gas phase. Subscripts *z* and *x* refer to vertical and horizontal direction respectively. Subscripts *i* and *j* refer to the solid species and gas species respectively. All other symbols are explained in the nomenclature. Further details on the formulation and solution method of Gpyro can be found in Lautenberger [20]. The thermo-physical properties of solid species and gas species were assumed to be constant. The gas-phase temperature was assumed to be the same as the condensed-phase temperature (thermal equilibrium).

$$\frac{\partial \rho}{\partial t} = -\dot{\omega}''_{fg} \tag{3}$$

$$\frac{\partial (\rho Y_i)}{\partial t} = \dot{\omega}''_{fi} - \dot{\omega}''_{di} \tag{4}$$

$$\frac{\partial(\rho h)}{\partial t} = k\frac{\partial}{\partial x}\left(\frac{\partial T}{\partial x}\right) + k\frac{\partial}{\partial z}\left(\frac{\partial T}{\partial z}\right) + \dot{\omega}''_{di}(-\Delta H_i) \tag{5}$$

$$\frac{\partial}{\partial t}\left(\rho_g \bar{\phi}\right) + \frac{\partial \dot{m}''_x}{\partial x} + \frac{\partial \dot{m}''_z}{\partial z} = \dot{\omega}''_{fg} \tag{6}$$

$$\frac{\partial}{\partial t}\left(\rho_g \bar{\phi} Y_j\right) + \frac{\partial}{\partial x}\left(\dot{m}''_x Y_j\right) + \frac{\partial}{\partial z}\left(\dot{m}''_z Y_j\right) = -\frac{\partial}{\partial x}\left(\bar{\phi}\rho_g D\frac{\partial Y_j}{\partial x}\right) - \frac{\partial}{\partial z}\left(\bar{\phi}\rho_g D\frac{\partial Y_j}{\partial z}\right) + \sum \dot{\omega}''_j \tag{7}$$

$$\dot{m}''_z = -\frac{\kappa}{\nu}\left(\frac{\partial p}{\partial z} - g\rho_g\right)\dot{m}''_x = -\frac{\kappa}{\nu}\frac{\partial p}{\partial x}\left(\rho_g = \frac{P\bar{M}}{RT}\right) \tag{8}$$

Previously, a 5-step reaction scheme had been proposed to simulate smouldering combustion of biomass fuels [7,22]. This scheme has shown validity in previous studies of peat wildfires through comparison to experimental data [8,19,22], and it was therefore used in the present study as well. The 5-step scheme includes a drying step (*dr*), a pyrolysis of peat (*pp*) and three parallel oxidative pathways: peat oxidation (*po*), *β*-char oxidation (*βo*) and *α*-char oxidation (*αo*) as shown in Eqs.(9) to (13)

$$\text{Peat} \bullet \nu_{w,dr}\text{H}_2\text{O} \rightarrow \text{Peat} + \nu_{w,dr}\text{H}_2\text{O(g)} \tag{9}$$

$$\text{Peat} \rightarrow \nu_{\alpha,pp}\,\alpha - \text{Char} + \nu_{g,pp}\text{Gas} \tag{10}$$

$$\text{Peat} + \nu_{O_2,po}\text{O}_2 \rightarrow \nu_{\beta,po}\beta - \text{Char} + \nu_{g,po}\text{Gas} \tag{11}$$

$$\beta - \text{Char} + \nu_{O_2,\beta o}\text{O}_2 \rightarrow \nu_{a,\beta o}\text{Ash} + \nu_{g,\beta o}\text{Gas} \tag{12}$$

$$\alpha - \text{Char} + \nu_{O_2,\alpha o}\text{O}_2 \rightarrow \nu_{a,\alpha o}\text{Ash} + \nu_{g,\alpha o}\text{Gas} \tag{13}$$

where $\nu_{w,dr}$ = MC and subscripts *w*, *p*, *α*, *β*, and *a* represent water, peat, *α*-char, *β*-char, and ash [7,8] respectively.

In Gpyro, the heterogeneous reaction *k* of condensed species *A* is represented in mass basis as shown in Eq. (13). The destruction rate of condensed species *A* in reaction *k* is expressed as Arrhenius law as shown in Eq. (A2) and Eq. (A3). The formation rate of condensed species *B* and all gases from reaction *k* are $\nu_{B,k}\dot{\omega}''_{dA_k}$ and $\dot{\omega}''_{fg_k} = (1-\nu_{B,k})\dot{\omega}''_{dA_k}$ [23]. The corresponding heat of reaction is $\dot{Q}''_k = -\dot{\omega}''_{dA_k}\cdot H_k$ [23]. Further details on the formulation of chemistry in Gpyro can be found in Lautenberger [20].

2.2. Boundary and initial conditions

By taking advantage of the geometrical symmetry of the experimental configuration in Christensen et al. [10], the computation domain was a half of the sample as shown in Fig. 2 to save computational resources and time.

The boundary conditions and initial conditions required are as follow: For the top free surface ($z = H$), a heat flux of $\dot{q}''_e = 200$ kW/m^2 was applied at the coil location ($x = 0 - 0.5$ cm) to simulate the heating of ignition protocol for the first 30 min (Eq.(14)). Both convective and radiative heat transfer were considered in the rest of the free surface Eqs. (14) to (16)). A heat transfer coefficient ($h_c = 10$ W/m^{2}K [24]) was used here and the emissivity (ε) of peat was set to 0.95 [7]. The gas transport on the free surfaces was calculated through Eqs.(17) and (18). The mass transfer coefficient (h_m) was calculated by $h_m = h_c/c_g$ according to mass-heat transport analogy [25], where the specific heat capacity for gas species (c_g) was assumed to be 1100 J/kg-K for all simulations [25]. For the bottom ($z = 0$), a convective heat transfer coefficient ($h_b = 0.5$ W/m^2-K) (Eq.(19)) was applied to account for the heat loss through insulating layer, which is within the range (0–3 W/ m^2-K)) reported in previous validated computational studies [7,9,17].

The impermeable boundary (Eq. (20)) was applied for the mass transfer of gas species at $z = 0$.

At the symmetrical plane and right wall (i.e $x = 0$ and $x = L/2$), adiabatic boundary condition (Eq.(A4)) was used for energy conservation equation and impermeable boundary condition (Eqs.(A5) and (A6)) for gas species.

$$-k\left.\frac{\partial T}{\partial z}\right|_{z=H,\ ig} = -\dot{q}''_e + h_c\left(T|_{z=H} - T_\infty\right) + \varepsilon\sigma\left(T^4|_{z=H} - T_\infty^4\right)\ (for\ t \leqslant 30\ \text{min}) \tag{14}$$

$$-k\left.\frac{\partial T}{\partial z}\right|_{z=H,\ ig} = h_c\left(T|_{z=H} - T_\infty\right) + \varepsilon\sigma\left(T^4|_{z=H} - T_\infty^4\right)\ (for\ t > 30\ \text{min}) \tag{15}$$

$$-k\left.\frac{\partial T}{\partial z}\right|_{z=H} = h_c\left(T|_{z=H} - T_\infty\right) + \varepsilon\sigma\left(T^4|_{z=H} - T_\infty^4\right) \tag{16}$$

$$-\psi\rho_g D\left.\frac{\partial Y_j}{\partial z}\right|_{z=H} = h_m\left(Y_j|_{z=H} - Y_j^\infty\right) \tag{17}$$

$$P|_{z=H} = P_\infty \tag{18}$$

$$-k\left.\frac{\partial T}{\partial z}\right|_{z=0} = -h_b\left(T|_{z=0} - T_\infty\right) \tag{19}$$

$$-\psi\rho_g D\left.\frac{\partial Y_j}{\partial z}\right|_{z=0} = 0 \tag{20}$$

The initial temperature for the sample and the air was 20 °C. The whole computational domain, including the pores inside the dust, has the same initial gas composition as the ambient air ($Y_O = 0.23$, and $Y_N = 0.77$).

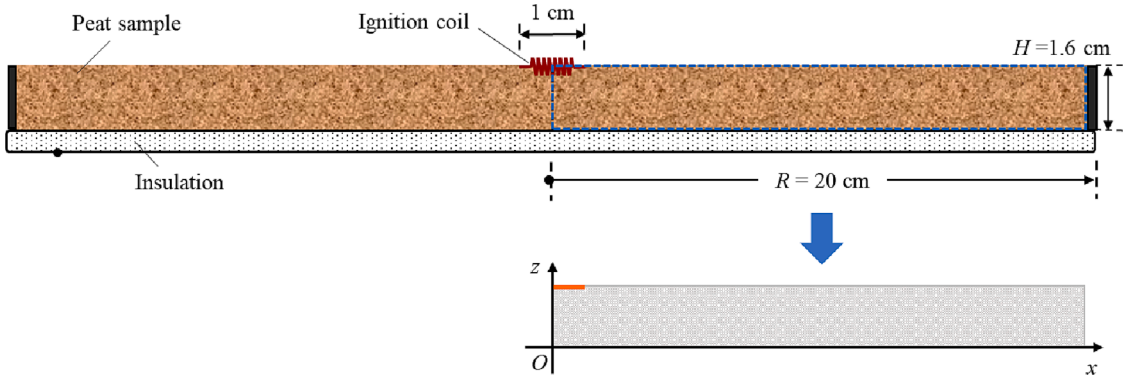

Fig. 2. Schematics for experimental set-up and two-dimensional computational domain.

2.3. Parameter selection

The chemical parameters of Huang et al. [7,22] for the 5-step reaction scheme of peat smouldering, which are the most comprehensive parameter values in the literature, were used here, and listed in Table 1.

The thermophysical properties of water, peat, α-char, β-char, ash, and sand are listed in Table 2. Except for sand, the thermo-physical properties for all the species were obtained from Huang et al. [7]. For sand, properties were obtained from similar sand types [26,27] except for bulk density (ρ_s) which was measured in Restuccia et al. [28] for the same sand in the experiments.

The thermophysical properties were assumed to be constant for the sake of simplicity. All gaseous species have unit Schmidt number, and equal free diffusion coefficient and specific heat. For mixed solid species, the averaged properties in each cell were calculated by weighting mass (Y_i) or volume fractions (X_i) as done in Lautenberger [20], where i refers to the species, for example, see Eq. (A7).

2.4. Validation and extrapolation use

Results from simulations in a shallow reactor were validated against the experiments of Christensen et al. [10]. These results consist of lateral spread rate (S_l), in-depth spread rate (S_d), and smouldering width (w). The determination of these outputs were based on leading and trailing edges. Leading edge is the first location of char oxidation (at the top surface of reactor) and trailing edge is the last location of char oxidation (at the bottom of reactor) [10]. The distance between the leading and trailing edges is referred to as smouldering width.

Lateral spread rate characterises the propagation of smouldering in the horizontal direction. Same as in Christensen et al. [10], here, the lateral spread rate was obtained by tracing the position of the leading edge at two different times: at 35 min (5 min after the end of ignition) and at the time at which the smouldering front reaches 17 cm from the igniter (3 cm from reactor walls) and then dividing the distance of these two positions by the time period.

In-depth spread rate was another key characteristic analysed in Christensen et al. [10]. Because in Christensen et al. [10] the thickness of peat is only 1.6 cm, S_d is hard to be directly measured in the shallow reactor; thus, it was calculated by dividing the thickness of the peat bed (H_0) by the burning time [10]. The burning time was defined as the time difference between the arrival of trailing edge and leading edge through a vertical profile [10]. We adapted this formulation to determine S_d in our predictions.

The experimental study in Christensen et al. [10] that used shallow reactor has limitations for in-depth spread rate because in a shallow reactor, it is not as meaningful as in a deeper reactor and the bottom boundary has a large influence on the in-depth spread [10,11]. We studied multi-dimensional smouldering in a deeper peat layer of thickness $H = 5$ cm. This thickness was selected because a thicker peat layer can facilitate the formation and collapse of overhang [13,18], and overhang is beyond the scope of the current paper. To model the igniter, we used greater heat flux and over a larger area ($\dot{q}''_{e,d} = 400$ kW/m^2 and $x = 0$–2 cm as in Eqs. (A8) and (A9)) to ensure a successful ignition. All other boundary conditions were the same as in the shallow reactor case.

In the deeper peat layer simulation, S_l was defined the same as that in the shallow reactor simulation. S_d was defined by tracing the time of arrival of the leading edge at the free surface and the time at which the trailing edge reaches 1 cm from bottom boundary, and then dividing the distance between these two positions by the time difference.

We also studied the effect of organic density in the deeper peat layer simulation. Organic density measures the amount of combustible material in a sample [10]. To study its effect, here we simulated the 2D smouldering of dry peat (with 0% MC and 0% IC) with organic density varying from 100 to 200 kg/m^3.

Previous experimental researches studied the influence of moisture and inorganic matters [9,10,16], but the individual influence for each of them has not be revealed. This is because in the experiments, adding moisture or inorganic matters also changes the organic density. What these experiments investigated was the coupling effect of organic density and moisture/inorganic matters. Thus, to reveal the individual influence of moisture or inorganic content on spread rate, here we used the 2D model in a deeper peat layer and fixed the value of organic density while varying the mass fraction of moisture or inorganic matters. Therefore, for the first time, the individual effects of MC and IC on multidimensional smouldering spread were investigated.

Table 1
Chemical parameters for the 5-step reaction scheme for peat [7], which consist of drying step (dr), pyrolysis of peat (pp), peat oxidation (po), β-char oxidation (βo), and α-char oxidation (αo).

Parameter	*dr*	*pp*	*po*	*βo*	*αo*
$\lg A_k$(lg (s^{-1}))	8.12	5.92	6.51	1.65	7.04
E_k(kJ/mol)	67.8	93.3	89.8	54.4	112
n_k(-)	2.37	1.01	1.03	0.54	1.85
$\nu_{B,k}$(kg/kg)	0	0.75	0.65	0.03	0.02
ΔH_k(MJ/kg)	2.26	0.5	−3.54	−19.5	−19.5
$\nu_{O_2,k}$(kg/kg)	0	0	0.27	1.48	1.49

Table 2
The values for thermophysical properties of all chemical species: of water, peat, α-char, β-char, ash, and sand.

Species (i)	$\rho_{s,i}$(kg/m^3)	$\rho_{o,i}$(kg/m^3)	ψ_i(-)	$k_{s,i}$(W/m-K)	$c_{p,i}$(J/kg-K)
Water	1000	1000	–	0.6	4186
Peat	1500	158	0.93	1.0	1840
α-Char	1300	135	0.90	0.26	1260
β-Char	1300	135	0.90	0.26	1260
Ash	2500	19.5	0.99	0.8	880
Sand	2500	1477	0.59	0.32	920

3. Results and discussions

3.1. Simulating smouldering in a shallow reactor

Arbitrarily, we choose a base case (MC = 40% and IC = 40%) to illustrate our simulations of the shallow-reactor in detail. Fig. 3 shows the temperature distributions in x and z planes at different times. During the ignition period (t = 1/4h), the temperature at the middle of the sample (left side in the computational domain) increased continuously and then reached a peak of 800 °C.

Smouldering started to spread at t = 1 h, forming a stable smouldering front at t = 2 h. The peak temperature and width of smouldering were nearly constant, reaching a semi-steady state. Smouldering eventually spread throughout the sample within 5 h, agreeing (~10% error) with the experimental observation in Christensen et al. [10]. Fig. 4 shows the predictions of transient 2D distributions for mass fractions of water (Y_w), peat (Y_p), and inorganic matters (Y_i) (sand and ash). During the ignition period (Fig. 4 (a)), the mass fraction of water decreased, then followed by the decrease of peat and the rose of ash. The changes in Y_w, Y_p, and Y_i represent the processes occurring at the smouldering front: peat drying, decomposition and oxidation, which has been discussed in previous studies [3,7,8,29].

The leading edge and trailing edge can be identified clearly in the stable smouldering front (Fig. 4 (c)). At the edges, Y_i = 100%, meaning at that point that the peat has burnt out. The leading edge corresponds to the surface and the trailing edge to the bottom of reactor (Fig. 4 (c)). The shape of the smouldering front agrees well with that reported in the experiments of Christensen et al. [10], and confirm with the shape in a field scale peat wildfire observed in Rein et al. [30]. It is worth noting that pyrolysis (Reaction (11) (12)) happens at lower temperatures than burning (Reaction (13) (14)). Once pyrolysis temperature reaches, peat

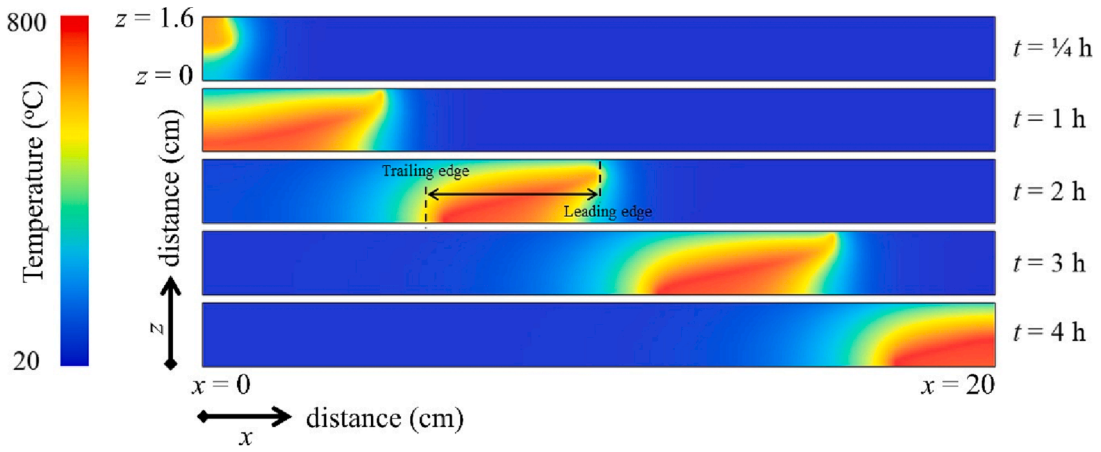

Fig. 3. Vertical profile of 2D temperature distributions at different times for base case simulation (IC = 40% and MC = 40%).

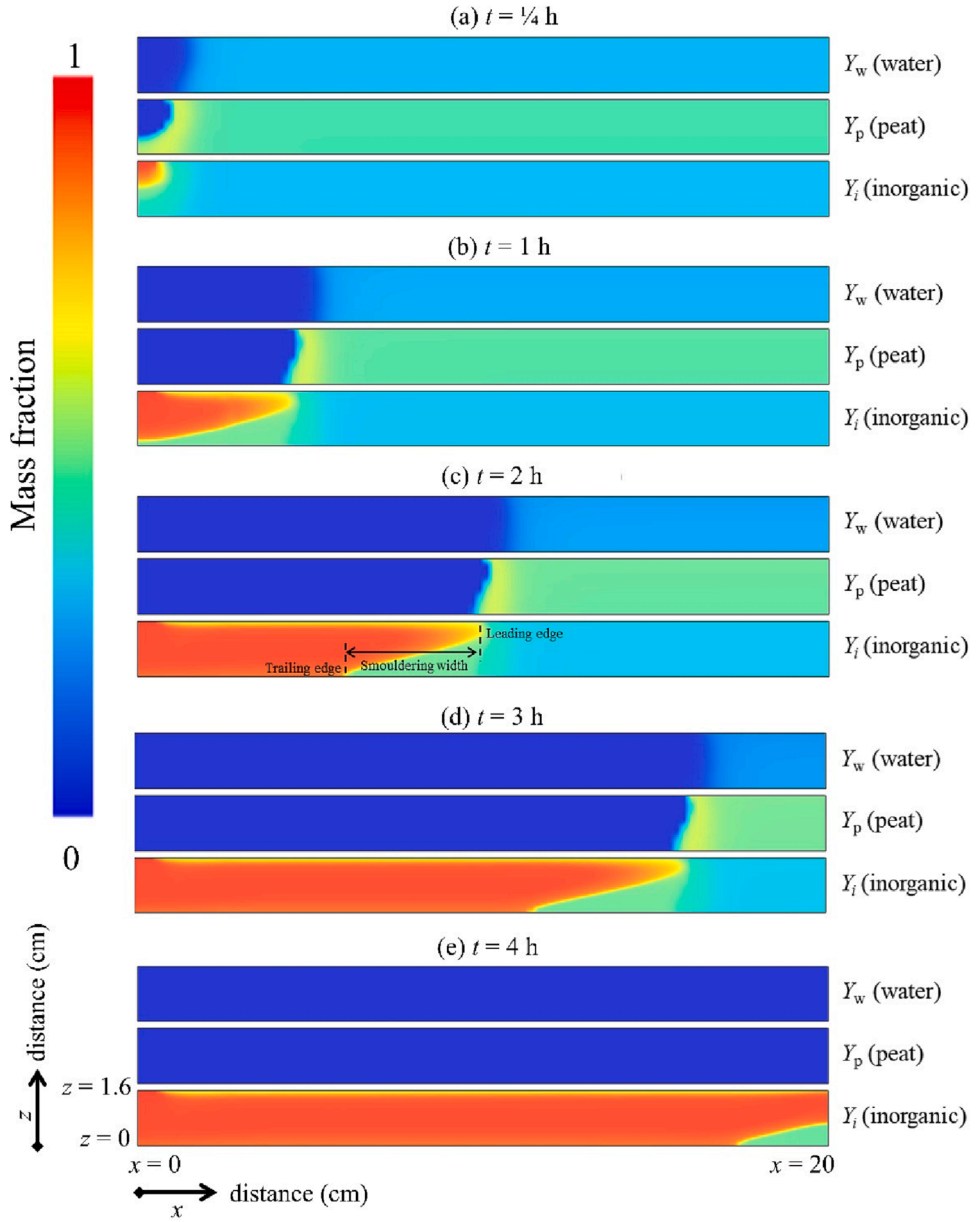

Fig. 4. Predictions of 2D distributions of mass fraction of water, peat, and inorganic matter at different times for base case simulation (IC = 40% and MC = 40%).

will pyrolyze into chars and Y_p will decrease to 0 rapidly, forming the edge $Y_p = 0\%$. This rapid change from peat to chars lead to a narrow width of edges $Y_p = 0\%$.

Fig. 5 summarizes the predicted S_l for different peat conditions and compares them with measurements in Christensen et al. [10]. Fig. 5(a) shows how S_l varies with MC. S_l decreases significantly with MC. For example, at MC = 0%, the predicted S_l was 12.6 cm/h and it decreased by 65% to 4.7 cm/h when MC increased to 140%. Our simulations have a reasonably good agreement with experimental data; the trends observed in the experiments were accurately predicted with an error of lower than 15% (relative absolute error). Fig. 5(b) shows the variation of S_l with IC; S_l decreased from 12.6 cm/h to 6.4 cm/h, as IC increased from 3% to 70%, which correspond to 20 – 25% error against experiments of Christensen et al. [10]. The predictions presented here are the average values, and due to the possible variations of physical parameters, the predictions have uncertainty of ± 25% [16].

The predicted *w* is summarised and compared with the experimental measurements of Christensen et al. [10] in Fig. 6. *w* decreased with IC and MC increased. The slope of *w vs.* MC has a decreasing trend with MC, whereas that of *w vs.* IC has an increasing trend with IC. Our predictions on *w* have good agreement with the experiments of Christensen et al. [10], with errors within 25%.

When smouldering approaches the extinction limits, the width reduced to a minimum of 1–2 cm. Our predictions of *w* at the extinction limits were around 20% higher than the measurement. This is because in the experiments of Christensen et al. [10], *w* was defined by an arbitrarily low threshold of upwards radiation, whereas we defined it by a temperature threshold (800 °C).

Fig. 7(a) shows that S_d increased with MC. At IC = 3%, it increases from 2.15 cm/h to 4.3 cm/h, when MC changes from 0% to 140%. At IC = 40%, S_d rises faster. S_d increases by 2 times, as MC increases from 0% to 70%. The findings agree with the previous research reported in [16]. Fig. 7(b) demonstrated that S_d stayed relatively stable as IC varied. This is because S_d denotes the burning rate, which decreases with the bulk organic density. Since moisture significantly deceases organic density of whole sample while sand does not change organic density much, the trends in Fig. 7(a) and (b) are therefore different [10,16].

Note that the predicted S_d (solid lines in Fig. 7) is lower than the measurements in Christensen et al. [10] (symbols in Fig. 7). This is due to the fact that the *w* was overpredicted, and this overprediction therefore resulted in an underprediction of $S_{d,}$. We found that in the MC case (left in Fig. 7) the average error against experiments is 26% and in the IC case (right in Fig. 7), it is 13%, which is of a reasonable accuracy. These findings show the ability of the 2D model to accurately predict multidimensional spread of smouldering; thus, improving previous 1D models [8,16]. With this multidimensional model, smouldering spread can be better understood than by using unidimensional models.

The in-depth spread rate of smouldering is limited by the oxygen supply [11]. Peatland has varying peat layer thickness, and a thicker peat layer has lower in-depth spread rate [11]. This was also simulated in this work and presented in the subsequent sub-section. However, a deeper peat layer simulated here is significantly shallower than the peat layer thickness in a real peatland (in the order of m [31]) to isolate the smouldering dynamics from overhang (see section 2.4), which is one limitation of the model.

3.2. Simulating smouldering in thicker peat layer

In the thicker peat layer simulation, the distributions of temperature and mass fraction of inorganic matter (Y_i) with IC(MC) = 40%(0%) are presented as an example (Fig. 8). We found that at $t = 0.5$ h (right after the ignition is off), the temperature at sample centre reached a high value due to the high heat flux during ignition; smouldering then spreads laterally and downwards. The lateral spread and in-depth spread can be identified in the contours of Y_i. We found that lateral spread is five to ten times faster than the in-depth spread. The vertical edge reached the bottom boundary at $t = 9$ h, when most of the samples has burn out.

Fig. 9(a) shows that both S_l and S_d decreased by 50 % as the organic density increased from 100 to 200 kg/m^3. The simulation results agree (within 20% error) with the measurements in previous experiments (MC = 0% and IC < 3%) [9,13,16].

Both the in-depth and lateral spread are essentially a burning process, and their rates are controlled by the rate of oxygen supply, as shown in Eq.(21) [16], where $\dot{m}''_b$ is the burning rate, $\dot{m}''_O$ is oxygen supply rate, υ_O is the chemical stoichiometry for oxygen, and ρ_{OC} is organic density, ρ_{air} is the air density, D_O is the diffusivity of oxygen, and $\frac{D_O}{l_g}$ is the characteristic air diffusion speed. When the oxygen supply ($\dot{m}''_O$) and stoichiometry is fixed, the burning rate is a constant. Therefore, the spread rate is inversely proportional to the organic (or fuel) density (spread rate $\propto 1/\rho_{OC}$), which can be demonstrated clearly in Fig. 9(b).

$$\text{Spread rate} = \frac{\dot{m}''_b}{\rho_{OC}} = \frac{\dot{m}''_O/\upsilon_O}{\rho_{OC}} \left(\dot{m}''_O = Y_O \rho_{air} \frac{D_O}{l_g}\right) \tag{21}$$

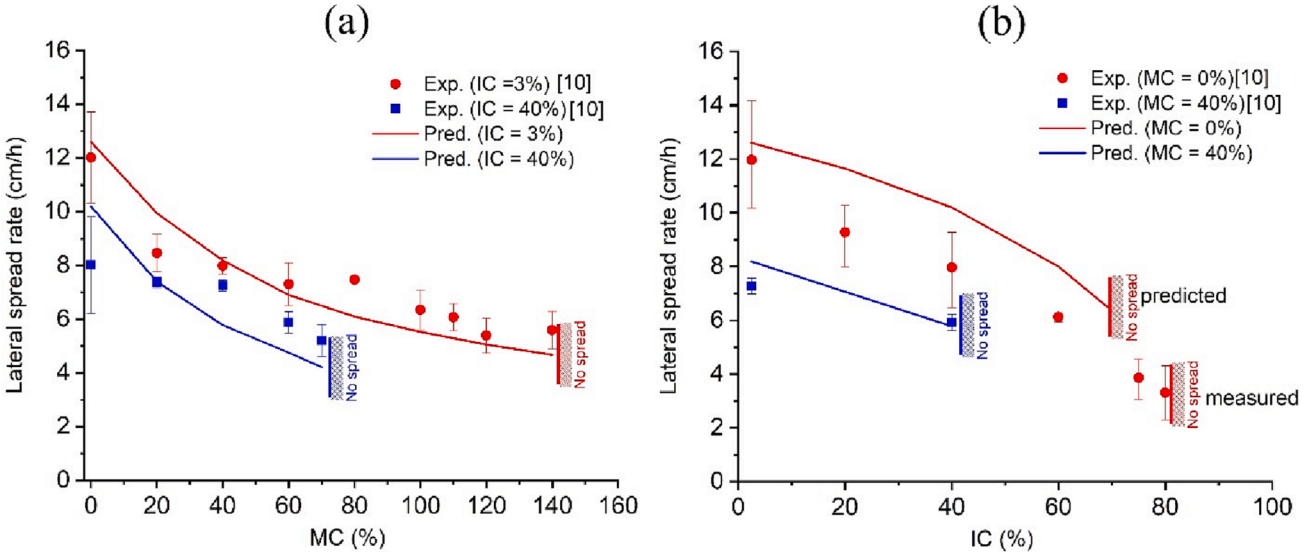

Fig. 5. Comparison of predicted and measured lateral spread rates: (a) versus MC; (b) versus IC. Lines represent predictions, symbols represent measurements in Christensen et al. [10], and error bars represent experimental uncertainties;

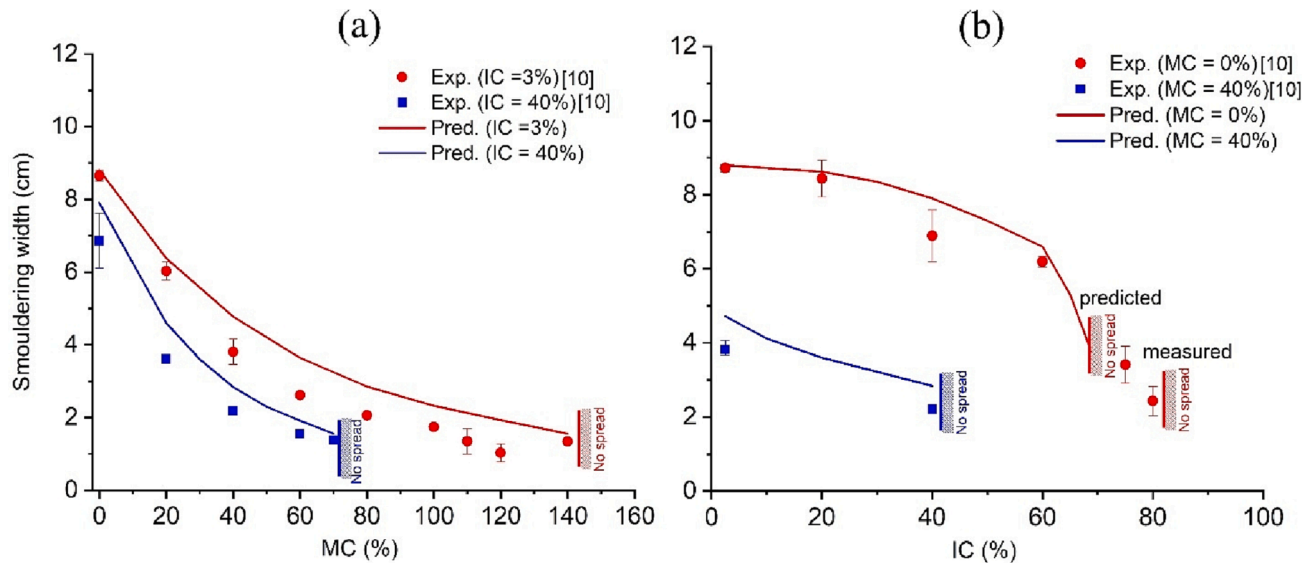

Fig. 6. Comparison of predicted and measured smouldering width: (a) versus MC; (b) versus IC. Lines represent predictions, symbols represent measurements in Christensen et al. [10], and error bars represent experimental uncertainties.

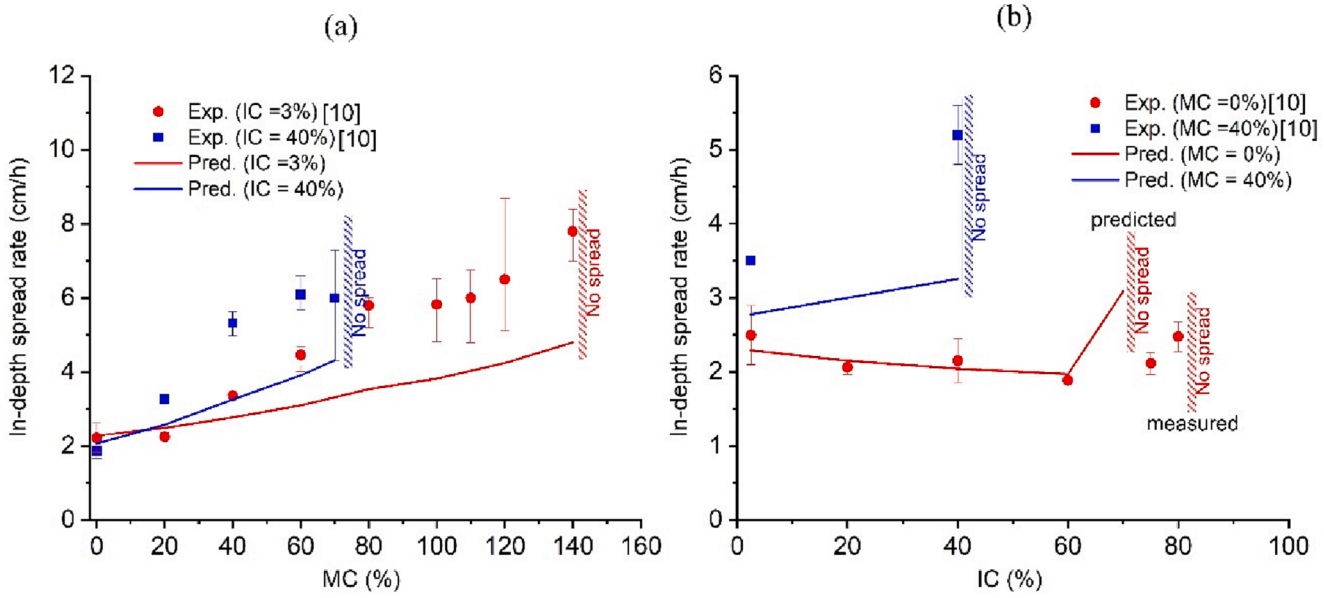

Fig. 7. Comparison of predicted and measured in-depth spread rates at different MCs and ICs: (a) versus MC; (b) versus IC. Solid lines represent predictions, symbols represent measurements in Christensen et al. [10], and error bars represent experimental uncertainties.

To better illustrate the influence of oxygen supply, we calculated the variation of S_l and S_d with the normalized diffusivity of oxidiser as shown in Fig. 10. It is seen that both lateral spread rate and in-depth spread rate are linearly correlated with the normalized diffusivity, which confirms the validity of Eq.(21) and further demonstrates that oxygen supply is a controlling mechanism in both lateral and in-depth spread.

Comparison shows that S_l is approximately 10–13 times greater than S_d as normalised diffusivity varies from 0.7 to 1.3. This is because oxygen supply for the near-surface lateral spread is significantly faster than in-depth spread. Although the environmental cooling for the lateral spread is also greater, the oxygen supply is the dominant factor that influences the smouldering spread rate, unless it is near the extinction limit [16,32]. However, the effect of changing diffusivity, thus changing oxygen supply, in lateral spread is 50% more significant than in in-depth spread, showing a higher sensitivity of lateral spread than in-depth spread towards the change of oxygen supply. Therefore the ratio of S_l to S_d varies with diffusivity, it increases from 10 to 13, as normalised diffusivity increases from 0.7 to 1.3.

Fig. 11(a) shows individual effect of MC and IC on lateral and in-depth spread rates. Solid lines demonstrate the effect of moisture (in the simulations IC is set to 0%), whereas dash lines demonstrate the effect of inorganic matters (in the simulations MC is set to 0%). It is seen that in terms of lateral spread, moisture has a significantly larger influence than inorganic matters. S_l decreases by ~ 60 % as the mass fraction of moisture (Y_w) increases from 0 to 40% whereas the same amount of increase in inorganic matter (Y_i) only brings about ~ 20% reduction of S_l.

Regarding in-depth spread, the influence of inorganic matters is slightly larger than moisture. S_d reduced by 27% as Y_i increased from 0 to 40% and by 20% as Y_w increased from 0 to 40%. This is because in-depth spread is more sensitive to oxygen diffusion inside peat sample

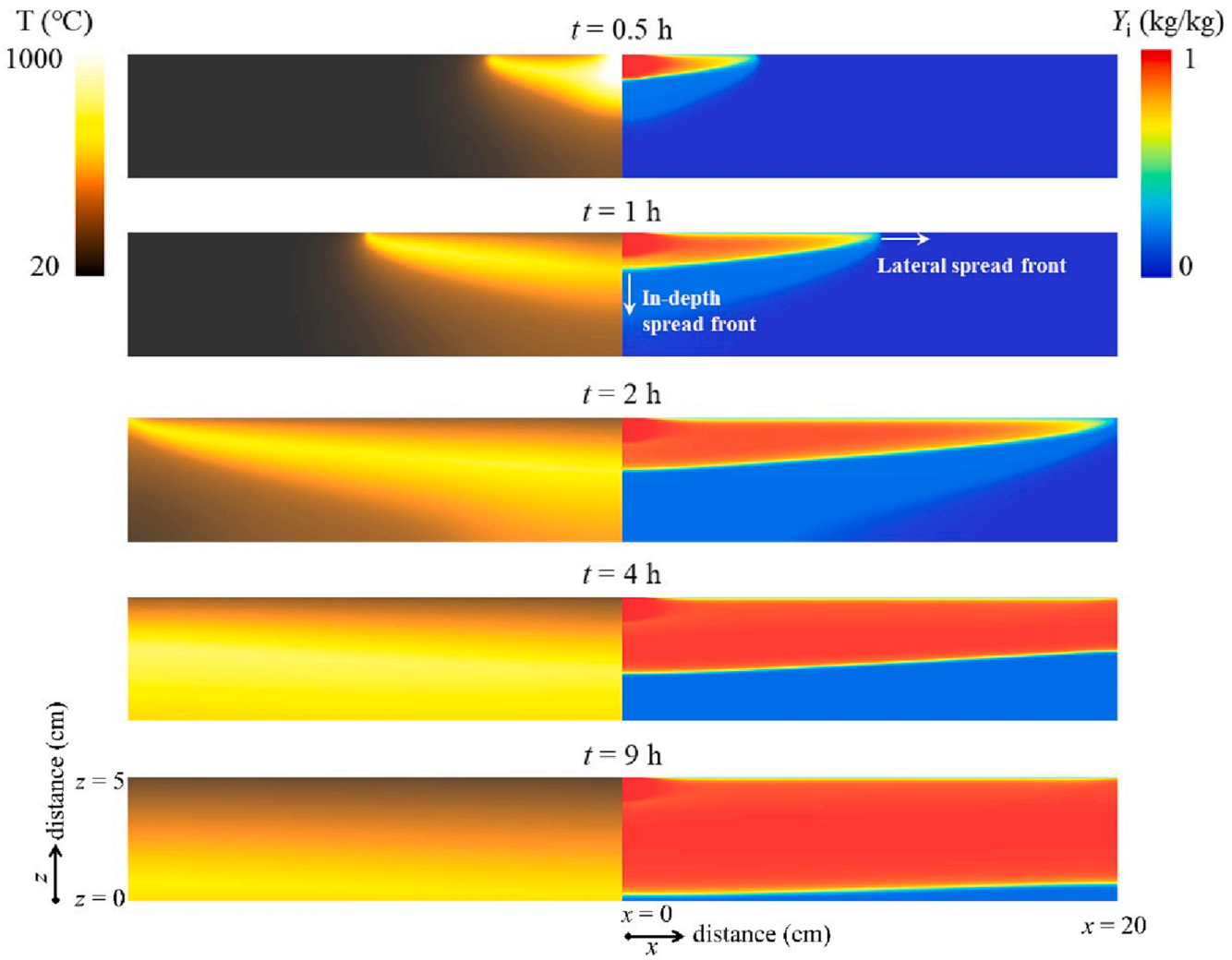

Fig. 8. 2D distributions of temperature and inorganic mass fraction at different times for the base case simulation with $H = 5$ cm (IC = 40% and MC = 0%). The left half is the contour of temperature and the right half is the contour of $Y_{i.}$

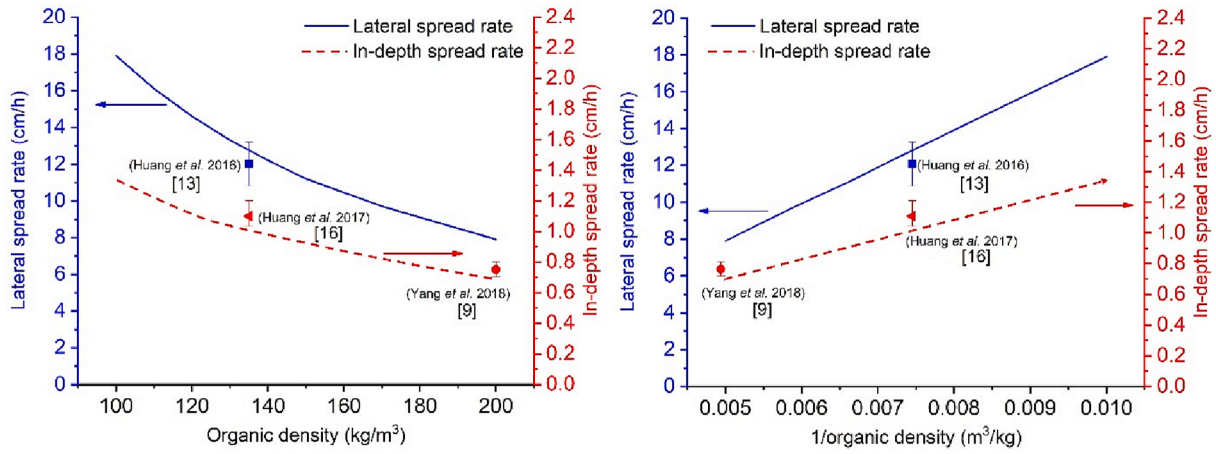

Fig. 9. Effect of organic density on lateral spread rate, S_l (blue, left y axis, see arrow direction) and in-depth spread rate, S_d (red, right y axis, see arrow direction). Experimental measurements from Huang et al., Huang and Rein, and Yang and Chen [9,13,16] are represented by symbols. The error bars represent the experimental uncertainties. (For interpretation of the references to colour in this figure legend, the reader is referred to the web version of this article.)

(beneath the free surface). The moisture inside the sample evaporates after drying and leaves the channels (pores) open to oxygen diffusion, while the inorganic matters stay during the whole smouldering process thus slowing down the diffusion of air inside the porous media [33,34].

The effect of inorganic matters and moisture on S_l/S_d is presented in Fig. 11(b). S_l/S_d stays relatively stable as Y_i varies because inorganic

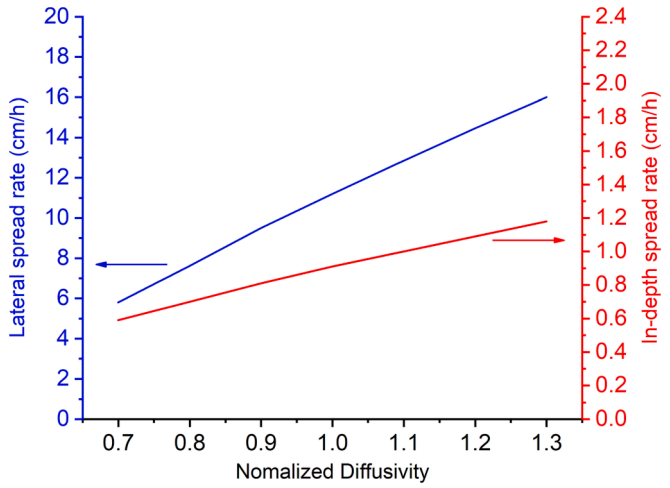

Fig. 10. S_l (blue, left y axis) and S_d (red, right y axis) *vs*. the normalized diffusivity of oxidiser. (For interpretation of the references to colour in this figure legend, the reader is referred to the web version of this article.)

matters have a similar effect on S_l and S_d. By comparison, S_l/S_d decreases by ~ 50% as Y_w increases from 0 to 40%, which is due to its significant influence on S_l.

It is noteworthy that the influence of inorganic density and moisture on lateral spread rate can be explained by a unified parameter, heat sink density [35]. Heat sink density (or thermal inertia, ΔH_T, see Eq.(A10)) is the amount of energy required to heat the soil to a typical peak smouldering, which can be defined as the enthalpy change, per unit volume, to a typical peak smouldering temperature for peat. The parameter values used in Eq. (A10) were obtained from Christensen [35], and shown in Table.

Fig. 12 demonstrates the relations between lateral spread and heat sink density. It is seen that there is highly correlated linearity between lateral spread rate and the inverse of heat sink density, with R^2 values of 0.97 for inorganic content and 0.98 for moisture content. This linear relation was also found in the experiments of Christensen, Hu et al., and Prat-Guitart et al. [35–37].

4. Conclusions

We computationally study the two-dimensional smouldering spread of peat at different conditions. Based on Gpyro, a two-dimensional model is built to simulate experiments conducted in a shallow reactor, and the model reasonably predicts the experiments of Christensen et al. [10] (average error of 20%). Based on the validated model, we further simulate a three times deeper layer. It is the first time that the lateral spread and in-depth spread of smouldering are simulated simultaneously. Due to the difference of oxygen supply at free surface and in-depth, the lateral spread is about 10 times faster than the in-depth spread. Besides, lateral spread rate has a strong linear correlation ($R^2 = 0.98$) with the inverse of heat sink density, which is the amount of energy required to heat the soil to

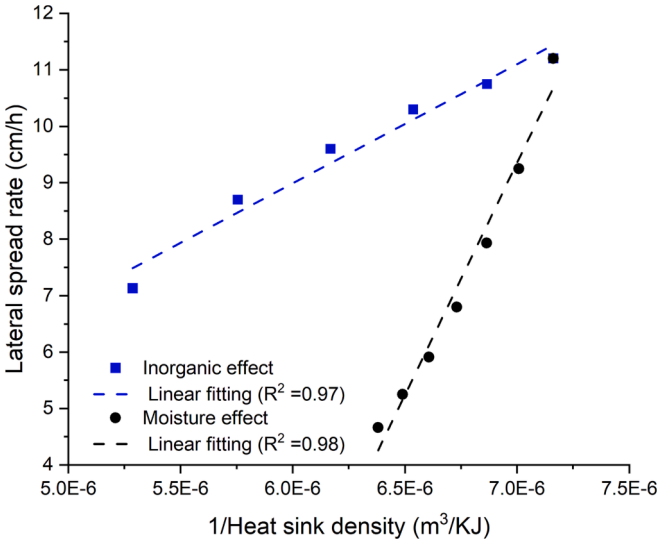

Fig. 12. Effect of heat sink on lateral spread rate obtained from the model predictions (symbols) and its linear fitting (dashed lines). Blue square symbols are inorganic effect and black round symbols are moisture effect. (For interpretation of the references to colour in this figure legend, the reader is referred to the web version of this article.)

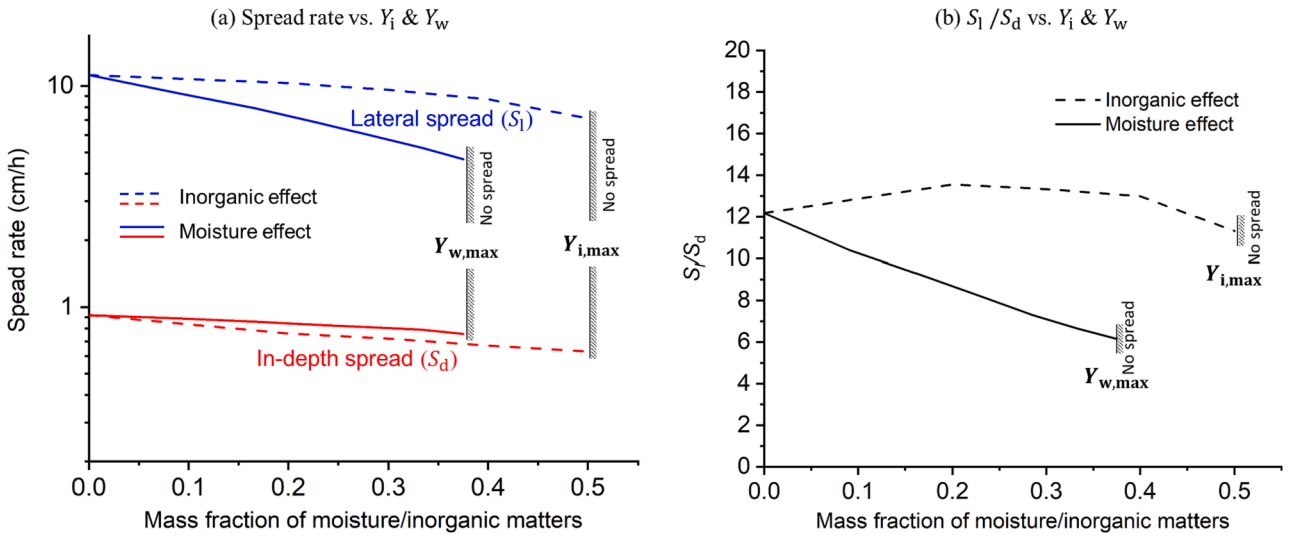

Fig. 11. Effect of moisture (Y_w) and inorganic matters (Y_i) on (a) lateral spread rate, S_l (blue) and in-depth spread rate, S_d (red); and (b) the ratio of S_l/S_d. Solid lines show the effect of moisture (no IC), and dash lines show the effect of inorganic matters (no MC). $Y_{w,max}$ and $Y_{i,max}$ refer to the ignition thresholds of water and inorganic matters. (For interpretation of the references to colour in this figure legend, the reader is referred to the web version of this article.)

peak smouldering temperature. The influence of inorganic density and moisture on lateral spread rate can be explained by this unified parameter, which confirms with the experimental results [35]. The findings help understand the controlling mechanism for multidimensional spread of smouldering peat wildfires and provide insights on this complex phenomenon, which is not well captured by previous 1D models [7,8,16]. These findings show the potential of the 2D model to improve understanding. With a model, the individual effect of peat conditions on multidimensional spread of smouldering can be investigated with a relatively low resources (for instance, compared to experimental study), advancing the studies on smouldering.

CRediT authorship contribution statement

Han Yuan: Validation, Investigation, Formal analysis, Conceptualization, Data curation, Methodology, Software, Visualization, Writing – original draft, Writing – review & editing. **Dwi M.J. Purnomo:** Formal analysis, Writing – review & editing. **Peiyi Sun:** Software, Methodology. **Xinyan Huang:** Writing – review & editing, Methodology, Software. **Guillermo Rein:** Conceptualization, Funding acquisition, Methodology, Software, Supervision, Writing – review & editing.

Declaration of Competing Interest

The authors declare that they have no known competing financial interests or personal relationships that could have appeared to influence the work reported in this paper.

Data availability

Data is available upon request.

Acknowledgements

This work was funded by European Research Council (ERC) Consolidator Grant HAZE (682587), HongKong RGC Postdoctoral Fellowship Scheme, National Natural Science Foundation of China (No. 51876183), and the President's PhD Scholarship Scheme of Imperial College London.

Appendix

$$A_k + \sum_{j=1}^{N} \nu'_{j,k} gas\ j \rightarrow \nu_{B,k} B_k + \sum_{j=1}^{N} \nu''_{j,k} gas\ j \tag{A1}$$

$$\dot{\omega}''_{dA_k} = \frac{(\rho Y_{A_k} \Delta z)_{\sum}}{\Delta z} A_k \exp\left(-\frac{E_k}{RT}\right) \left(\frac{\rho Y_{A_k} \Delta z}{(\rho Y_{A_k} \Delta z)_{\sum}}\right)^{n_k} Y_{O_2}^{n_{O_2,k}} \tag{A2}$$

$$(\rho Y_i \Delta z)_{\sum} \equiv (\rho Y_i \Delta z)\,|_{t=0} + \int_0^t \dot{\omega}''_{fi}(\tau) \Delta z(\tau) d\tau \tag{A3}$$

$$-k \left.\frac{\partial T}{\partial x}\right|_{x=0,L/2} = 0 \tag{A4}$$

$$-\bar{\psi} \rho_g D \left.\frac{\partial Y_j}{\partial x}\right|_{x=0,L/2} = 0 \tag{A5}$$

$$\left.\frac{\partial P}{\partial x}\right|_{x=0,L/2} = 0 \tag{A6}$$

$$\bar{c} = \sum Y_i c_i,\ \bar{\rho} = \sum X_i \rho_i, \bar{k} = \sum X_i k_i \tag{A7}$$

$$-k \left.\frac{\partial T}{\partial z}\right|_{z=H,\ 0cm \leqslant x \leqslant 2cm} = -\dot{q}''_{e,d} + h_c\left(T|_{z=H} - T_\infty\right) + \varepsilon\sigma\left(T^4|_{z=H} - T_\infty^4\right) (0 \leqslant t \leqslant 30\ \text{min}) \tag{A8}$$

$$-k \left.\frac{\partial T}{\partial z}\right|_{z=H,\ 0cm \leqslant x \leqslant 2cm} = h_c\left(T|_{z=H} - T_\infty\right) + \varepsilon\sigma\left(T^4|_{z=H} - T_\infty^4\right) (t > 30\ \text{min}) \tag{A9}$$

$$\Delta H_T = \rho_{\text{bulk}} \left\{ (Y_i c_i)(T_{\text{sm}} - T_0) + Y_O[(T_{\text{sm}} - T_0) c_O + \Delta H_p)] + Y_w[c_{ev}(T_{ev} - T_0) + \Delta H_{ev}] \right\} \tag{A10}$$

Equation developed in [35] where T_{sm} is the smouldering temperature, T_{ev} is the temperature of evaporation, ΔH_p is the heat of pyrolysis, and ΔH_{ev}

Table A1
List of values used for calculating heat sink density.

Variable	Value	Unit	Description
c_w	4186	J/kg·K	Specific heat of water
c_o	1840	J/kg·K	Specific heat of organic matter
c_i	920	J/kg·K	Specific heat of inorganic matter
T_0	20	°C	Initial temperature
T_{ev}	100	°C	Temperature of water evaporation
T_{sm}	550	°C	Temperature increase to peak value in smouldering
ΔH_{ev}	2256	kJ/kg	Latent heat of water vaporisation
ΔH_p	500	kJ/kg	Heat of pyrolysis

is the heat of evaporation.

References

[1] Rein G. Smouldering fires and natural fuels. Chapter 2 Fire Phenom Earth Syst – An Interdiscip Approach to Fire Sci 2013:15–34.
[2] Ohlemiller TJ. Modeling of smoldering combustion propagation. Prog Energy Combust Sci 1985;11:277–310.
[3] Rein G. Smoldering combustion. SFPE Handb Fire Prot Eng Fifth Ed 2016;1:581–603. https://doi.org/10.1007/978-1-4939-2565-0_19.
[4] Turetsky MR, Benscoter B, Page S, Rein G, Van Der Werf GR, Watts A. Global vulnerability of peatlands to fire and carbon loss. Nat Geosci 2015;8:11–4.
[5] Freeman C, Evans CD, Monteith DT, Reynolds B, Fenner N. Export of organic carbon from peat soils. Nature 2001;412:785.
[6] Page SE, Siegert F, Rieley JO, Boehm HDV, Jaya A, Limin S. The amount of carbon released from peat and forest fires in Indonesia during 1997. Nature 2002;420:61–5. https://doi.org/10.1038/nature01131.
[7] Huang X, Rein G, Chen H. Computational smoldering combustion: predicting the roles of moisture and inert contents in peat wildfires. Proc Combust Inst 2015;35:2673–81.
[8] Huang X, Rein G. Computational study of critical moisture and depth of burn in peat fires. Int J Wildl Fire 2015;24:798. https://doi.org/10.1071/wf14178.
[9] Yang J, Chen H. Natural Downward Smouldering of Peat : Effects of Inorganic Content and Piled Bed. Fire Technol 2018. https://doi.org/10.1007/s10694-018-0737-8.
[10] Christensen EG, Fernandez-Anez N, Rein G. Influence of soil conditions on the multidimensional spread of smouldering combustion in shallow layers. Combust Flame 2020;214:361–70. https://doi.org/10.1016/j.combustflame.2019.11.001.
[11] Christensen EG, Hu Y, Purnomo DMJ, Rein G. Influence of wind and slope on multidimensional smouldering peat fires. Proc Combust Inst 2020. https://doi.org/10.1016/j.proci.2020.06.128.
[12] Rein G, Huang X. Smouldering Wildfires in Peatlands, Forests and the Arctic: Challenges and Perspectives. Curr Opin Environ Sci Heal (under Rev 2021.
[13] Huang X, Restuccia F, Gramola M, Rein G. Experimental study of the formation and collapse of an overhang in the lateral spread of smouldering peat fires. Combust Flame 2016;168:393–402. https://doi.org/10.1016/j.combustflame.2016.01.017.
[14] Frandsen WH. Ignition probability of organic soils. Can J For Res 1997;27:1471–7.
[15] Frandsen WH. The influence of moisture and mineral soil on the combustion limits of smoldering forest duff. Can J For Res 1987;17:1540–4.
[16] Huang X, Rein G. Downward spread of smouldering peat fire: the role of moisture, density and oxygen supply. Int J Wildl Fire 2017;26. 10.1071/wf16198.
[17] Yang J, Chen H, Liu N. Modeling of two-dimensional natural downward smoldering of peat. Energy Fuel 2016;30:8765–75.
[18] Yang J, Liu N, Chen H, Gao W, Tu R. Effects of atmospheric oxygen on horizontal peat smoldering fires: Experimental and numerical study. Proc Combust Inst 2018. https://doi.org/10.1016/j.proci.2018.06.218.
[19] Huang X, Rein G. Upward-and-downward spread of smoldering peat fire. Proc Combust Inst 2019;37:4025–33.
[20] Lautenberger C. Gpyro3D: A three dimensional generalized pyrolysis model. Fire Saf Sci 2014;11:193–207.
[21] Mulky TC, Niemeyer KE. Computational study of the effects of density, fuel content, and moisture content on smoldering propagation of cellulose and hemicellulose mixtures. Proc Combust Inst 2019;37:4091–8. https://doi.org/10.1016/j.proci.2018.06.164.
[22] Huang X, Rein G. Smouldering combustion of peat in wildfires: Inverse modelling of the drying and the thermal and oxidative decomposition kinetics. Combust Flame 2014;161:1633–44.
[23] Lautenberger C. Gpyro-A Generalized Pyrolysis Model for Combustible Solids: Technical Reference. Berkeley: 2014.
[24] Wu D, Schmidt M, Berghmans J. Spontaneous ignition behaviour of coal dust accumulations: A comparison of extrapolation methods from lab-scale to industrial-scale. Proc Combust Inst 2019;37:4181–91.
[25] Lautenberger C, Fernandez-Pello C. Generalized pyrolysis model for combustible solids. Fire Saf J 2009;44:819–39.
[26] Somerton WH. Some thermal characteristics of porous rocks. Pet Trans 1958;213:375–8.
[27] Kiyohashi H, Sasaki S, Masuda H. Effective thermal conductivity of silica sand as a filling material for crevices around radioactive-waste canisters. High Temperaure-High Press 2004;35:179–92.
[28] Restuccia F, Huang X, Rein G. Self-ignition of natural fuels: Can wildfires of carbon-rich soil start by self-heating? Fire Saf J 2017;91:828–34.
[29] Lin S, Sun P, Huang X. Can peat soil support a flaming wildfire? Int J Wildl Fire 2019;28:601–13. https://doi.org/10.1071/wf19018.
[30] Rein G, Cleaver N, Ashton C, Pironi P, Torero JL. The severity of smouldering peat fires and damage to the forest soil. Catena 2008;74:304–9.
[31] Hayasaka H, Usup A, Naito D. New Approach Evaluating Peatland Fires in Indonesian Factors. Remote Sens 2020;12. 10.3390/rs12122055.
[32] Lin S, Huang X. Quenching of smoldering: Effect of wall cooling on extinction. Proc Combust Inst 2020. https://doi.org/10.1016/j.proci.2020.05.017.
[33] Yuan H, Restuccia F, Rein G. Computational study on self-heating ignition and smouldering spread of coal layers in flat and wedge hot plate configurations. Combust Flame 2020;214:346–57. https://doi.org/10.1016/j.combustflame.2019.12.041.
[34] Yuan H, Restuccia F, Rein G. Spontaneous ignition of soils: A multi-step reaction scheme to simulate self-heating ignition of smouldering peat fires. Int J Wildl Fire 2021;30:440–53. https://doi.org/10.1071/WF19128.
[35] Christensen E. Experimental Investigation of the Effects of Soil and Environmental Conditions on Smouldering Wildfires. Imperial College London, 2020.
[36] Hu Y, Christensen E, Restuccia F, Rein G. Transient gas and particle emissions from smouldering combustion of peat. Proc Combust Inst 2019;37:4035–42.
[37] Prat-Guitart N, Rein G, Hadden RM, Belcher CM, Yearsley JM. Propagation probability and spread rates of self-sustained smouldering fires under controlled moisture content and bulk density conditions. Int J Wildl Fire 2016;25:456–65.